*J Mater Sci*

**Energy materials**

# Novel air-electrode materials for low-cost inert-supported solid oxide cells: investigation of materials compatibility during co-sintering

M. M. Juckel[1,*], F. Grimm[1], S. Zischke[2], Y. J. Sohn[1], O. Guillon[1,3], and N. H. Menzler[1]

[1] *Forschungszentrum Jülich GmbH, Institute of Energy and Climate Research, Materials Synthesis and Processing (IEK-1), 52425 Jülich, Germany*

[2] *Central Facility for Electron Microscopy (GfE), RWTH Aachen University, Aachen, Germany*

[3] *JARA-Energy, Jülich, Germany*

**Received:** 19 April 2023
**Accepted:** 13 August 2023



## ABSTRACT

For the investigation of the reactivity of alternative solid oxide cell air electrode materials with forsterite ($Mg_2SiO_4$), a magnesium silicate doped with Zn and Ca, five different phase materials were chosen: two Ruddlesden–Popper phase materials: $La_4Ni_3O_{10}$ (L4N3) and $La_3Ni_2O_7$ (L3N2) and three titanium-based perovskite materials: $SrTiO_3$ (STO), $SrTi_{0.75}Fe_{0.25}O_3$ (STF25) and $CaTi_{0.9}Fe_{0.1}O_3$ (CTF). Forsterite was chosen as a support material for the fuel cell, as it is abundant and therefore relatively inexpensive. For the investigation of their reactivity, different types of samples were prepared: mixed pellets, double-layered pellets and screen-printed electrode inks on forsterite green substrates, which were subsequently co-sintered at $T = 1300$ °C. These samples and their cross sections were then studied using XRD, SEM, EDS and TEM lamella point analysis. Consequently, the impedance spectra were acquired to determine their electro-catalytic performance. The two Ruddlesden–Popper phase materials L4N3 and L3N2 are of high interest due to their thermodynamic stability and high electro-catalytic activity, resulting in a very low polarization resistance. However, this polarization resistance is increased when mixing with forsterite material. In case of the three titanium-based perovskites, the electro-catalytic activity is of less interest due to high polarization resistances.

Handling Editor: Kyle Brinkman.

Address correspondence to E-mail: m.juckel@fz-juelich.de

https://doi.org/10.1007/s10853-023-08862-0
Published online: 05 September 2023

## Introduction

In 1958, Ruddlesden and Popper synthesized a special perovskite structure with the general formula of $A_{n+1}B_nO_{3n+1}$ [1, 2]. The structure of these so-called Ruddlesden–Popper phases consists of $nABO_3$ layers which are sandwiched between two AO rock salt layers along the crystallographic *c*-axis. This results in a different amount of perovskite polyhedral units, which determine the phase of the materials. In case of the first member of this family ($n = 1$), the $K_2NiF_4$ is adopted with a rare or alkaline earth element on the A-site and transition or post-transition metals on the B-site. Within this structure, A-site cations are surrounded by 9 oxygen atoms, which are located at the boundary between the two types of layers. The B site cations, on the other hand, have a coordination number of six and an occupied center of an apically elongated $BO_6$ octahedra with two slightly longer apical B–O bonds along the *c*-axis and four other basal plane B–O bonds [3].

It is the similarity of Ruddlesden–Popper phase materials to common perovskites, which makes them interesting in different research areas. They can be used as ferroelectrics [4, 5], colossal magnetoresistance materials [6], mixed ionic and electronic conductors [7], thermoelectrics or high $T_C$ superconductors [8]. Some of the first member of the Ruddlesden–Popper phase materials have even been used as alternatives for air-electrode applications in solid oxide fuel cells (SOFCs) and solid oxide electrolysis cells (SOECs) [9].

In this, Ruddlesden–Popper phase materials are mainly used in air-electrode applications for intermediate temperature SOFCs (IT-SOFCs; T = 500–700 °C). This leads to a variation of different advantages compared to conventional SOFCs using $La_{1-x}Sr_xMnO_{3-\delta}$ (LSM) or $La_{1-x}Sr_xCo_{1-y}(Fe_y)O_{3-\delta}$ (LSC(F)) and operating at higher temperatures ($T \geq 700$ °C). Among others, there are lower operational costs, less interface reactions between cell components and less electrode phase transitions, both leading to a better long-term performance [10]. Furthermore, these rare-earth nickelates have high electro-catalytic activity under oxidizing conditions [10–12], high mixed ionic and electronic conductivity (MIEC) [13–15] as well as moderate temperature expansion coefficient (TEC) [11]. The latter turned out to be especially advantageous when mixing with ceria-based electrolyte GDC (gadolinia-doped ceria; *cp.* $La_4Ni_3O_{10-\delta}$ ($13.2 \times 10^{-6}$ $K^{-1}$) vs. GDC ($13.4 \times 10^{-6}$ $K^{-1}$)) [11, 16]. In case of $La_2NiO_{4+\delta}$ (L2N1), however, its use as air-electrode material is limited by its low electronic conductivity, especially compared to common LSM or LSCF. While various attempts of doping on the A-site and/or the B-site of L2N1 to increase its low electronic conductivity have been made, the use of high-ordered Ruddlesden–Popper phases has shown more promising results [11, 17–21]. This can be explained by the fact that with a higher number of $NiO_6$-octahedrons, the concentration of Ni–O–Ni bonds increases, which are in charge of electronic conduction pathways of perovskite layers [22]. Indeed, $La_4Ni_3O_{10-\delta}$ (L4N3) is a metallic conductor at room temperature [12]. It is the relatively high abundance of reported L2N1 publications as well as the improved electronic conductivity, which made us focus on the research of $La_3Ni_2O_{7-\delta}$ (L3N2) and $La_4Ni_3O_{10-\delta}$ (L4N3) as new Ruddlesden–Popper phases for electrode applications.

For the use of these Ruddlesden–Popper phase materials in solid oxide fuel cells (SOFCs), inert-supported cells (ISCs) were chosen for mainly two reasons. Firstly, these kinds of cells using cheap porous materials as a support, which makes them very cost-effective. Secondly, lower ohmic losses and lower operating temperatures are possible due to the thin, supported electrolyte [23]. In comparison with that, the today's state-of-the-art cells, e.g., fuel-electrode supported cells (FESCs), electrolyte-supported cells (ESCs) and metal-supported cells (MSCs), are less beneficial as they are on the way to market via industrialization with the actual air electrodes performing well. In case of FESCs, the cells possess a low overall resistance, which is caused by a relatively thick but porous support and anode layer (> 200 µm) (low gas diffusion resistance) making it consequently possible to apply an electrolyte with a rather low thickness (2–20 µm), resulting here, again, in low ohmic losses and therefore high performance and subsequently aiming for low operating temperatures [24]. However, after each manufacturing step, a sintering step is typically needed, which increases the manufacturing costs [25]. ESCs, on the other hand, have a relatively thick electrolyte layer of typically > 80 µm, in order to give the cells mechanical stability. Due to this thick electrolyte layer, the ohmic resistance is increased and the cells must be operated at high temperature (around or above 800 °C). Nevertheless, the ESC design has the advantage of very low leakage rate [24]. Finally, the biggest advantage of MSCs is the use of relatively cheap metals, like Fe- or Cr-based ones,

for the stability of the cells [26]. Moreover, the operating temperatures of MSCs are rather low (600 °C in the case of Ceres Power) [27]. The biggest disadvantage of MSCs is the manufacturing process, as the sintering of the cells have to be performed in a reducing atmosphere or vacuum in order to prevent corrosion, or the functional layers have to be applied by physical methods like sputtering/physical vapor deposition which increases the manufacturing costs. Furthermore, interdiffusion between the metal support and the anodic nickel plays a crucial role, while oxide scale formation at high water vapor pressures might be problematic for the long term [28, 29].

Herein, we investigate the reactivity of unusual Ruddlesden–Popper phase materials in inert-substrate-supported solid oxide fuel cells. Therefore, forsterite ($Mg_2SiO_4$), an abundant and cheap manganese silicate, was chosen as support material on the air side of the SOFC. In this context, a variety of cathode material phases have already been investigated and reported previously [30–32]. Furthermore, three more titanium-based perovskite phases were used for comparison regarding performance, microstructure and possible formation of foreign phases and / or reaction layers to check their applicability to SOCs with respect to reactivity and electrochemistry. These are $SrTiO_3$ (STO), $SrTi_{0.75}Fe_{0.25}O_3$ (STF25) and $CaTi_{0.9}Fe_{0.1}O_3$ (CTF). While STO is known to be very stable, especially when it comes to sulfur poisoning, STF25 and CTF were chosen to investigate the influence of Fe on the B-site and the elimination of Sr compared to STO, respectively.

## Experimental

L4N3 and L3N2 were prepared via Pechini method in which stoichiometric amounts of the respective nitrates (lanthanum nitrate hexahydrate [$La(NO_3)_3{\cdot}6H_2O$; 99.99%; Alfa Aesar], strontium nitrate hexahydrate [$Sr(NO_3)_2{\cdot}6H_2O$; 99%; Sigma-Aldrich], and calcium nitrate tetra hydrate [$Ca(NO_3)_2{\cdot}4H_2O$; 99%; Alfa Aesar]) were dissolved in deionized water. Consequently, calculated amounts of citric acid (20% excess) and ethylene glycol were added. After evaporation of the water at 350 °C, a gel was formed and dried overnight. Once dried, organic residue were removed at 650 °C and temperatures of 1040 °C for 4 h (L4N3) and 950 °C for 8 h (L3N2), respectively, were used for calcination [33, 34]. STF25 was synthesized by a modified Pechini synthesis, CTF was prepared by liquid-phase synthesis and STO was commercially obtained by Sigma-Aldrich [35]. Pellets of 22 mm diameter of each composition were made by pressing 2 g of the respective electrode powders with forsterite in a 50:50 ratio, applying 5kN for 2 min. For the investigation of high temperature stability, these pellets were sintered between 1100 and 1300 °C with heating and cooling rates of 3 K / min and 5 K / min, respectively. The overall stoichiometric compositions $(A_{0.58}A'_{0.4})B_{0.2}B'_{0.8}O_3$ were kept constant to avoid possible influences of different compositions.

To simplify the interaction of forsterite with the complex Ruddlesden–Popper phases and the titanium-based perovskite cathode materials, the respective single oxides were also investigated. Therefore, $La_2O_3$ [Sigma-Aldrich, 99.99%] and SrO [Sigma-Aldrich, 99.99%] were screen-printed on the forsterite substrate and CaO [Chem-Pur, 99.99%] and $Fe_2O_3$ [Sigma-Aldrich; ≥ 99%] were pressed into double-layered pellets with the same settings as described above. These pellets were subjected to the standard heat treatment program (T = 1300 °C for 5 h).

A Bruker AXS X-ray diffractometer with Bragg–Brentano configuration and CuK$\alpha$ radiation was used for phase-purity determination and structural characterization. Furthermore, inductively coupled plasma optical emission spectrometry (ICP-OES) was used for verifying the real final composition of the powder (Table 1).

For the determination of the polarization resistance ($R_{pol}$) of each electrode material, electrochemical

**Table 1** Calculated composition (ICP-OES) and synthesis method of different cathode materials

| Electrode | Calculated composition (acc. to ICP-OES) | Synthesis method |
|---|---|---|
| L4N3 | $La_{4.01\pm0.12}Ni_{2.99\pm0.09}O_{10}$ | Pechini |
| L3N2 | $La_{3\pm0.09}Ni_{2\pm0.06}O_7$ | Pechini |
| STO | $Sr_{0.986\pm0.030}Ti_{1.014\pm0.030}O_3$ | Commercially available |
| STF25 | $Sr_{1.048\pm0.031}Ti_{0.68\pm0.021}Fe_{0.263\pm0.008}O_3$ | Modified pechini |
| CTF | $Ca_{1.012\pm0.030}Ti_{0.890\pm0.026}Fe_{0.100\pm0.002}O_3$ | Liquid-phase synthesis |

impedance spectroscopy (EIS) was performed on symmetrical cells. Therefore, an Alpha A high-performance frequency analyzer (Novocontrol Technologies) at a frequency range between $10^6$ and $10^{-1}$ Hz and a voltage of 20 mV was used. However, only the polarization resistance ($R_{pol}$) is of interest within this research, as the ohmic resistance ($R_{ohm}$), for instance, is affected by the device itself and/or by the quality of the material with which the sample is contacted. Therefore, Nyquist plots were obtained from the EIS measurements, whereby the ohmic resistance ($R_{ohm}$) was subtracted from it. By doing so, EIS offers the opportunity to visualize, in terms of $R_{pol}$ values, the influence of the formation of secondary phases—irrespective of whether they are due to reactions with forsterite or electrode decomposition—as well as the impact of the low-cost co-firing manufacturing route (in terms of microstructural changes and co-firing capability of the electrode materials), thereby allowing air-electrode benchmarking.

For the investigation of the electrochemical measurements, the electrode samples were prepared as followed: 8YSZ substrates (200 µm, Kerafol) were screen-printed with a GDC barrier layer (Wet layer thickness = 35 µm) and consequently sintered at $T$ = 1300 °C for 3 h. The subsequent electrode layer ($D$ = 12 mm, wet layer thickness = 65 µm) and the current collector layer (CCL), consisting of 50 wt% $La_{0.65}Sr_{0.3}MnO_3$ (LSM) and 50 wt% transport medium (pure or mixed with 20% forsterite) was then screen-printed on top ($D$ = 12 mm, wet layer thickness = 2 × 173 µm) and fired between $T$ = 1100° and 1300 °C (Fig. 1). The measurement of the particle size was taken by a Horiba LA 950 V2 Analyzer (Retsch Technology GmbH, Haan, Germany), and the viscosity was measured with a rheometer (Anton Paar MCR 301) at a shear rate of 109 $s^{-1}$. Moreover, to investigate the reactivity toward forsterite, inks of these materials were screen-printed on a forsterite green (non-sintered) plate, an inert magnesium silicate ($Mg_2SiO_4$) doped with Zn and Ca, with same screen printing settings. The ink itself, consisted of 62.75 wt% electrode powder, 20.85 wt% $\alpha$-terpineol (DuPont) and 16.4 wt% TM (transport medium containing 6 wt% 45 cp ethyl cellulose and $\alpha$-terpineol). The particle size and ink viscosity are summarized in Table 2.

The cross-sectional surfaces of the samples were investigated with a scanning electron microscope (SEM) (Zeiss Ultra55 with EDS from Oxford Instruments; INCAEnergy400) and then polishing with silica suspension. To ensure sufficient electrical conductivity, the different specimens were sputtered with platinum. For the preparation of TEM specimens, a carbon protective layer was first applied using vapor deposition on the surface of the sample. Subsequently, the

**Table 2** Particle size of the powder of different electrode materials

| Electrode | Laser diffraction analyzer (µm) | | | Ink viscosity at 109 $s^{-1}$ (Pa*$s^{-1}$) |
|---|---|---|---|---|
| | $d_{(10)}$ | $d_{(50)}$ | $d_{(90)}$ | |
| L4N3 | 0.42 | 0.70 | 1.57 | 8.9 |
| L3N2 | 0.60 | 0.80 | 1.04 | 7.0 |
| STO | 0.30 | 0.90 | 2.46 | 7.9 |
| STF25 | 0.52 | 0.80 | 1.22 | 15.4 |
| CTF | 0.59 | 0.82 | 1.13 | 13.1 |

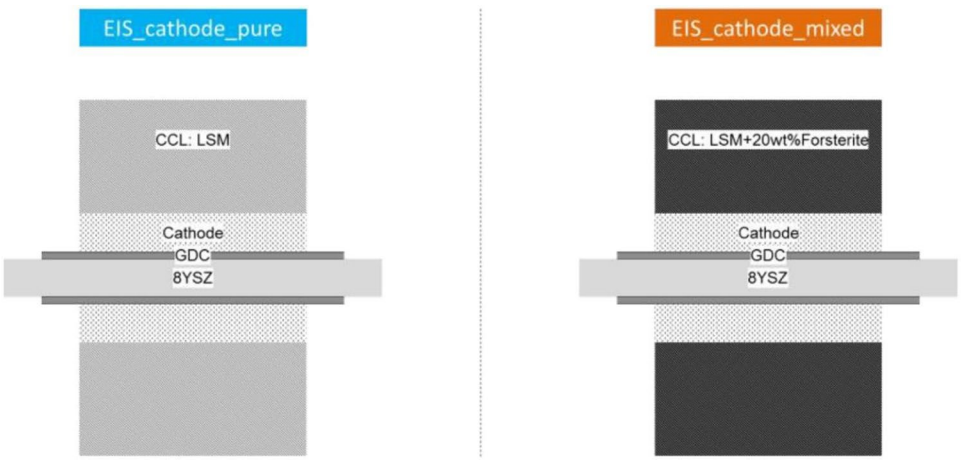


**Figure 1** Symmetrical cell design for the samples with a pure LSM CCL (EIS_cathode_pure) and mixed LSM + 20 wt% forsterite CCL (EIS_cathode_mixed).

protective layer was cut from both sides using a Ga ion beam (accelerating voltage of 30 kV). Afterward, the sample plate is tilted 45° to the ion beam to allow cutting of the underside of the sample. To remove the lamella, the fragile sample is attached to a finely extended tungsten needle with a sputtering layer of platinum. This allows the lamella to be carefully removed from the sample. The lamella has the following sample dimensions: length ≈ 12 µm; height ≈ 5 µm and thickness ≈ 150 nm. For the FIB sample preparation, the Strata 400 s instrument (Thermo Fisher Scientific, USA) was used.

## Results and discussions

### High temperature stability of the electrode and SEM characterization

In a first step, each of the five materials was investigated by heat treatment up to $T = 1200$ °C. Only the two Ruddlesden–Popper phase materials L4N3 and L3N2 show formation of secondary phases at higher temperatures. Indeed, while L3N2 shows the formation of L2N1, L4N3 is completely transformed into L3N2. Additionally, here, again, L2N1 as well as NiO is formed (The determination of the foreign phases has been determined by comparing with ICSD). This can be probably explained by the increased thermodynamical stability of Ruddlesden–Popper phases with increasing order of n (Fig. 2) [36]. Consequently, L3N2 seems to be more likely kinetically stable and favorably formed at higher temperatures. The lattice parameter of L3N2, which crystallize in the space group *Amam*, changes only a bit in the *c-axes* before ($a = 5.4(6)$, $b = 5.4(6)$, $c = 20.4(2)$) and after ($a = 5.451(9)$, $b = 5.404(9)$, $c = 20.52(6)$) heat treatment.

In the next step, the interaction of the different electrode materials with forsterite was investigated to demonstrate the reaction tendency of the different materials within these combinations. Therefore, the electrode–forsterite samples were analyzed, whereby the particle size of the inks were not kept constant. Consequently, no further analytics concerning the porosity visible in the following figures were performed.

Figure 3 shows the interaction of the different electrodes with forsterite. The reactivity of these five materials can be divided into three groups. While STO only shows a limited formation of foreign phases in the electrode layer as well as in the forsterite phase, during co-firing at $T = 1300$ °C, the two other titanium-based perovskites STF25 and CTF show the highest reactivity. Here, reaction layers with different thicknesses are revealed in the two phases as well as on the interface. That means that STO is the most stable phase with the lowest reactivity within this investigated family of titanium-based perovskites. The two Ruddlesden–Popper phase materials, on the other hand, show a moderate reactivity toward the forsterite material, resulting in foreign phases along the electrode–forsterite interface

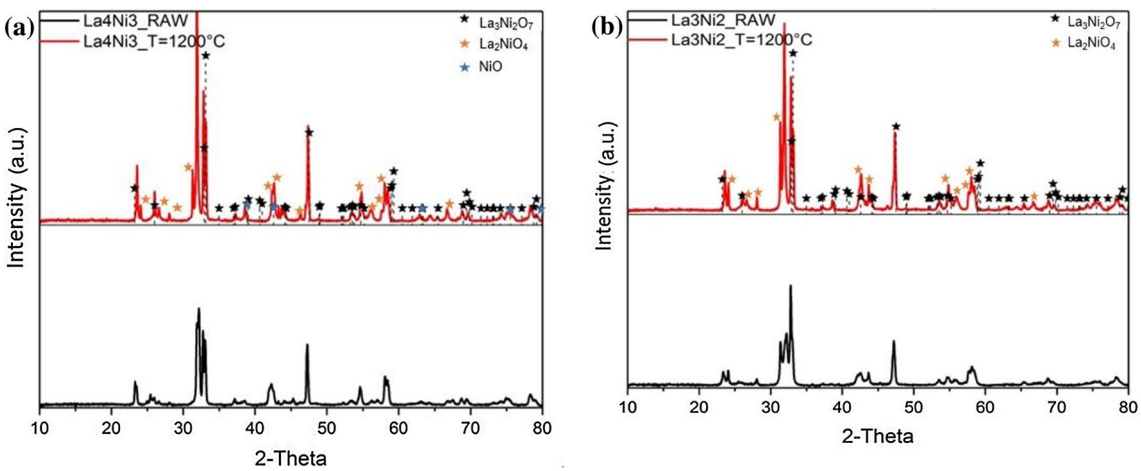


**Figure 2** XRD for **a** L4N3 raw and L4N3-only pellet and **b** L3N2 raw and L3N2-only pellet. The comparison shows that L4N3 has some impurities of L3N2 at higher temperatures. The other diffractograms are displayed in Supplementary 1 (The determination of the foreign phases has been determined by comparing with ICSD).

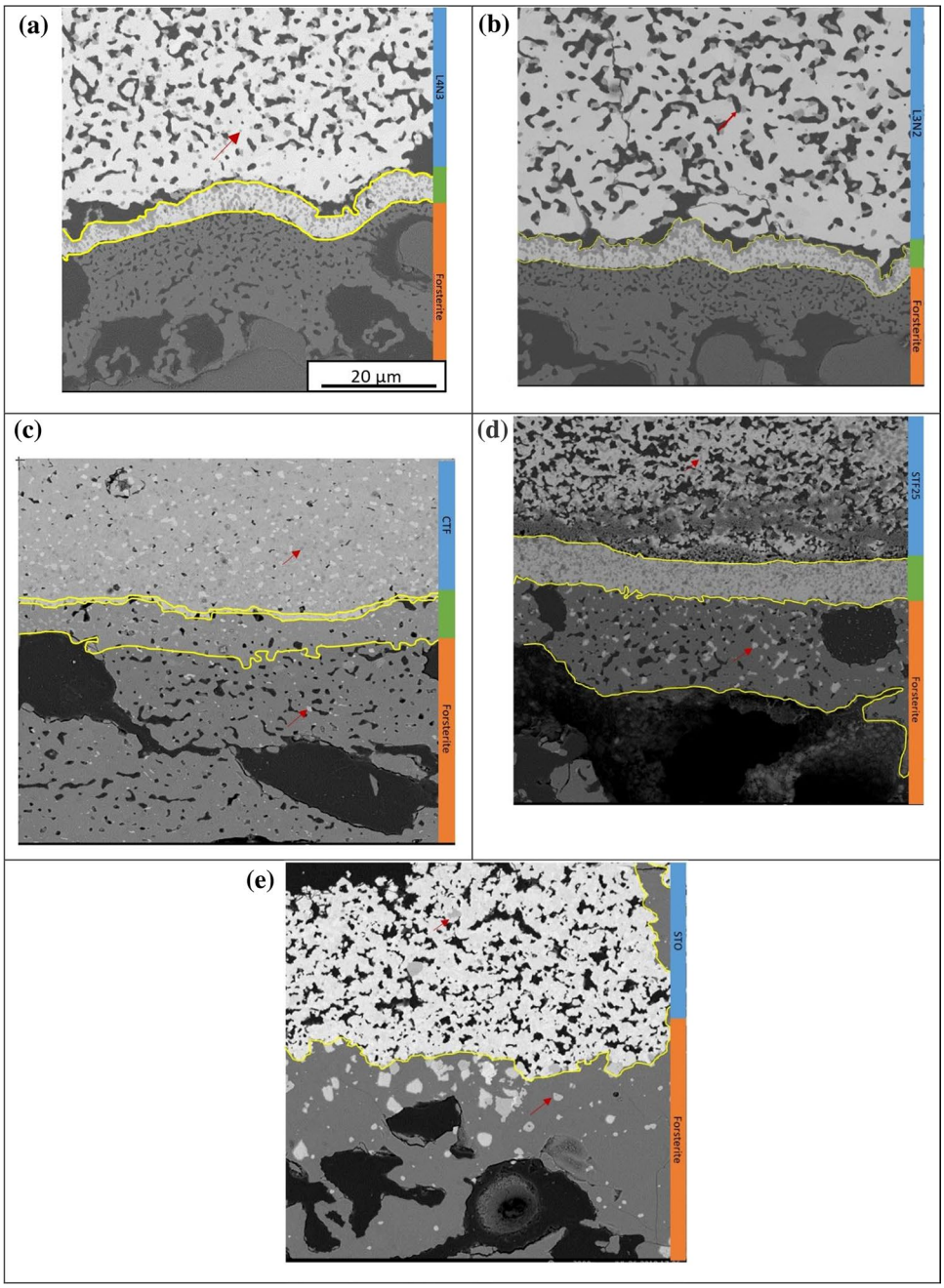


**Figure 3** SEM cross sections after screen printing of cathode–forsterite samples with: **a** L4N3, **b** L3N2, **c** CTF, **d** STF25, **e** STO on forsterite. For **a–d**, the cross sections show a very strong reaction and the formation of reaction layers. In contrast, **e** shows only some foreign phases. Reaction layers are highlighted in yellow; foreign phases indicated with a red arrow. (For interpretation of the references to color in this figure legend, the reader is referred to the Web version of this article).

as well as in the electrode layer itself. However, there are no further foreign phases in the forsterite phase, which is different compared to STF25 and CTF with the highest reactivity.

## Qualitative diffusive study by EDS

As depicted in Fig. 3, all the electrode materials show a certain reactivity toward forsterite, resulting in the formation of different reaction layers and / or several foreign phases. For a further insight into the diffusion tendency of the different electrode and forsterite elements, energy-dispersive X-ray spectroscopy (EDS) was performed on the embedded, ground and

polished electrode–forsterite samples. The results of these measurements can be seen in Fig. 4. Additional EDS maps for the titanium-based perovskite-forsterite are displayed in Supplementary 2.

Alongside the cross section of Fig. 4, the major elements of the support material forsterite are highlighted in brown: Mg, Si and Zn (excluding Ca). The respective elements of the Ruddlesden–Popper phase materials (highlighted in blue) are listed: La and Ni. Both measurements (SEM cross section: Fig. 3 and EDS cross section: Fig. 4) show the presence of several foreign phases along the electrode–forsterite interface as well as in the electrode phase.

In case of forsterite, the elements of this phase show a diffusion gradient resulting in less visible signals of Mg, Zn and Si with increasing distance from the material. It should be noted that the three elements itself display different tendency for its diffusion. In that, Zn has the highest diffusion tendency resulting in Zn signals in the entire electrode (50 µm) as well as Zn-rich foreign phases. This diffusion is based on gas phase diffusion and has been discussed in more detail by Matte et al. in a previous publication [30]. In addition, the majority of Zn appears to be located inside the thin reaction layer. Mg and Si, on the other hand, can only be found in the forsterite phase and along the forsterite–electrode layer. Moreover, neither Mg nor Si shows strong tendency for diffusion, and the majority of the two elements remain inside the support material itself. The elements of the Ruddlesden–Popper phase material, on the other hand, barely show any tendency in diffusion. The signal of La and Ni is only visible in the electrode layer and beneath the reaction layer. This is congruent with the fact that Ruddlesden–Popper phases are admittedly catalytically active but mostly thermodynamically stable.

Due to the little reactivity, further investigation of the Ruddlesden–Popper phase materials has been undertaken with TEM lamella point analysis (Fig. 5).

The analysis of the L3N2-forsterite sample covers the whole range from the substrate forsterite, the interdiffusion layer to the electrode L3N2 (L4N3 and L3N2 show similar reactivity and consequently only L3N2 is shown). The TEM lamella point analysis shows that four different foreign phases, which can be found within the substrate forsterite, the foreign phases and the electrode phase, contain Zn. Furthermore, Fig. 5 shows the following result: The concentration of Ni in the electrode phase is very low and the concentration of La within the area of foreign phases is low, too. The concentration of Mg, on the other hand, is the highest within these foreign phases, compared to the other metal phases (see Table 3).

## Phase analysis after heat treatment by XRD

After sintering each of the electrode–forsterite combinations, several foreign phases and reaction layers were observed. In order to get more precise quantification of these phases, XRD measurements were taken for each combination of the electrode–forsterite samples. Therefore, electrode mixed pellets were produced and the corresponding diffractograms are shown in Fig. 6. At the bottom of the graph, the

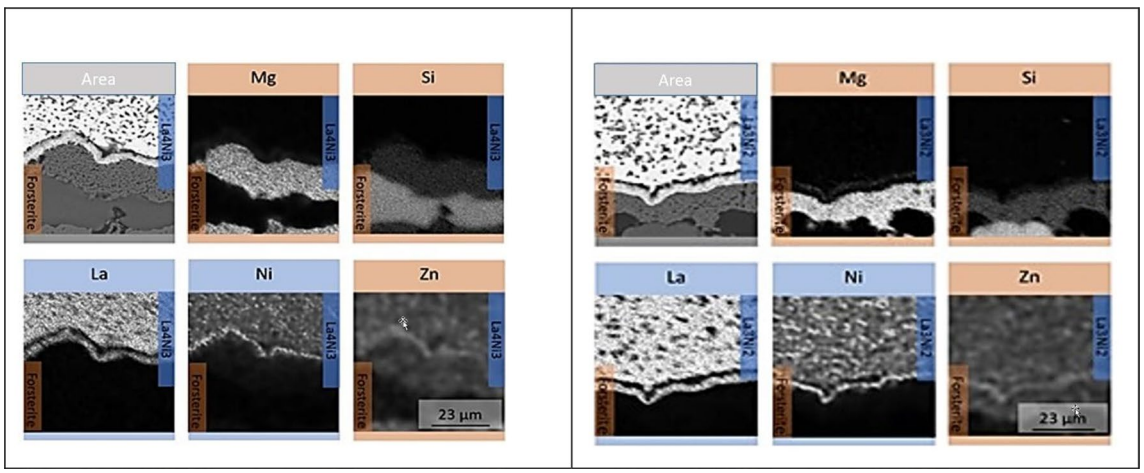


**Figure 4** EDS (Mg, Zn, La, Ni, and Si) mapping from L4N3- and L3N2-forsterite. The brightness is correlated to the concentration of the elements. Regions appearing as black do not contain any traces of the respective element.

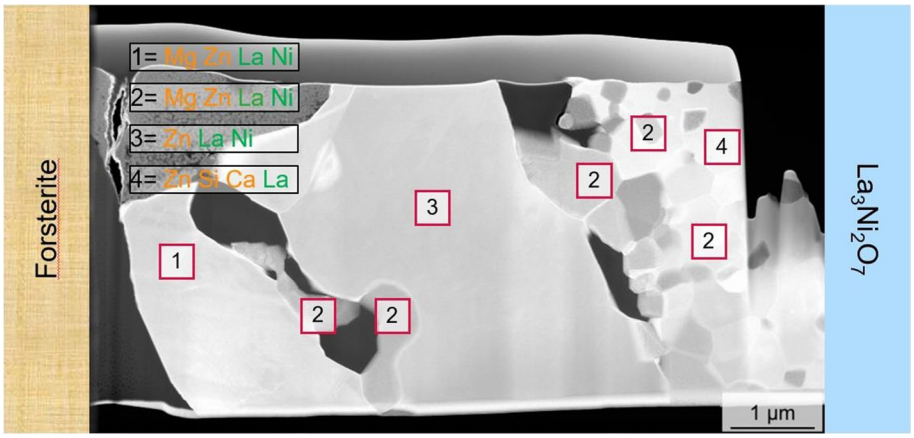


**Figure 5** STEM-DF lamella point analysis of L3N2-forsterite (black spots are pores). The foreign phases are described in the upper left corner.

**Table 3** Atom% in the different phases

| Elements | Electrode phase (%) | Foreign phase (%) |
|---|---|---|
| La | 45 | > 1 |
| Ni | > 1 | 40 |
| O | 35 | 25 |
| Mg | 18 | 16 |
| Zn | > 1 | 18 |

respective diffractogram of the raw electrode material and the raw forsterite material are highlighted in blue and black, respectively. In the upper part of the graph, the electrode mixed pellet of the respective electrode and forsterite sintered at $T = 1300$ °C for 5 h is shown in grey. The several foreign phases, which are formed after sintering, are identified and denoted by stars. In general, the XRD measurements confirm the results from EDS measurements: Both Ruddlesden–Popper phases L4N3 and L3N2 show lower reactivity toward the forsterite material, compared to the other cathode materials tested. However, in both cases $La_9Mg_{0.5}Si_6O_{26}$ and in case of L4N3 additional $La_2NiO_{4.003}$ has been detected (Fig. 6). In case of the titanium-based perovskites, the reactivity toward forsterite is also in good agreement with the results of the EDS measurements. However, STO-forsterite does not show any foreign phases compared to the results of the EDS measurements. This is probably caused by the detection limit of the XRD machine, which has to be at least 1.5wt%, depending on the preparation of the sample and the surrounding matrix composition. The two other titanium-based perovskites show the foreign phases $Fe_2MgO_4$ and $Sr_2Mg(Si_2O_7)$ (for STF25) and $CaMgSiO_4$ (for CTF), respectively. Structure-wise, these two foreign phases $Sr_2Mg(Si_2O_7)$ and $CaMgSiO_4$

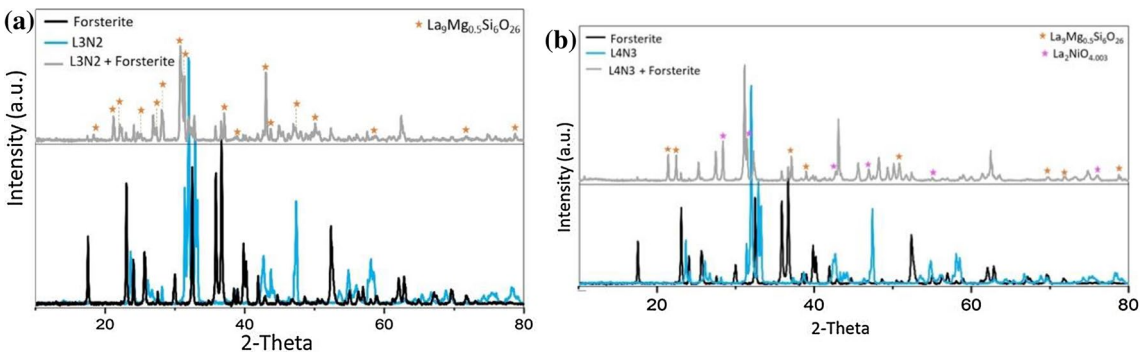


**Figure 6** XRD for **a** L4N3-forsterite and **b** L3N2-forsterite (in grey; mixed pellet) after $T = 1300$ °C for 5 h. The patterns are shown for raw forsterite (black line) and for the raw electrode material (blue line). (For interpretation of the references to color in this figure legend, the reader is referred to the Web version of this article) (The determination of the foreign phases has been determined by comparing with ICSD).

are similar, with the exception of Ca occupying the A-site (instead of Sr), and consequently interacting with Si and Mg from forsterite. Both show the strong reactivity and diffusion tendency of Sr and Si. The results of the XRD measurements are summarized in Table 3 and the XRD can be found in the supplementary information. (The determination of the foreign phases has been determined by comparing with ICSD).

The majority of these foreign phases contain Sr and Si. Moreover, based on the EDS mappings (*cf.* Fig. 4), the electrode forsterite combinations are also expected to form more Zn-containing phases. However, none of the XRD measurements, could confirm this result, which is probably due to the small amount of Zn compared to Si.

## Reactivity of different oxides with the support material by EDS and XRD

Individual oxide interaction tests were performed with $La_2O_3$, SrO, $Fe_2O_3$, CaO and NiO as basic oxides for perovskites, to investigate the strong reaction of forsterite to a single element visible in Fig. 7 and in the Supporting Information 3. Furthermore, additional XRD measurements were taken and are depicted in Fig. 8, which shows two different diffractograms: At the bottom of the graph, the diffractogram of the individual raw oxide material and the raw forsterite

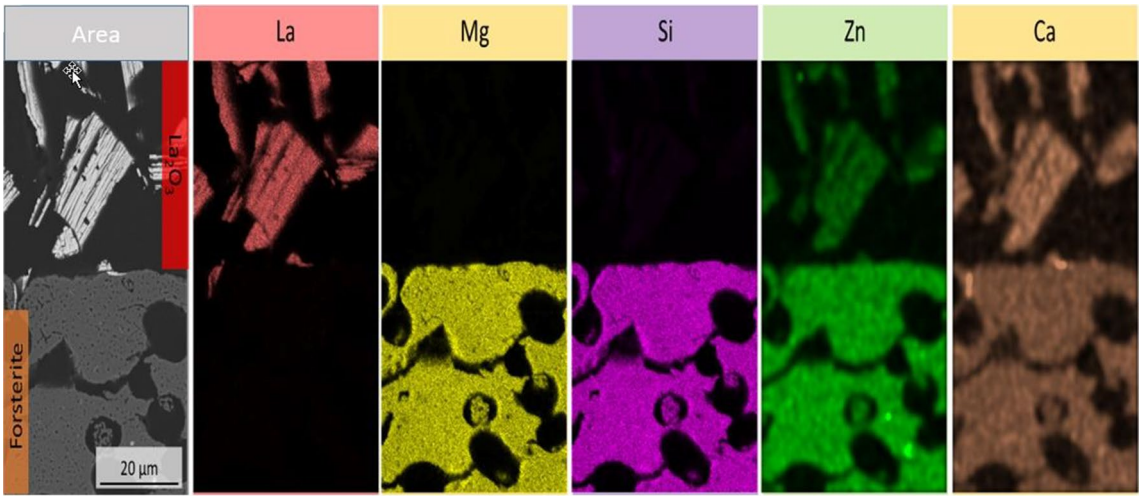


**Figure 7** EDS mapping of the oxide double-layered pellet sample: $La_2O_3$ double-layered pellet. Two layers are visible. They differ considerably with respect to their Mg and Zn content, which is visualized by the EDS mapping.

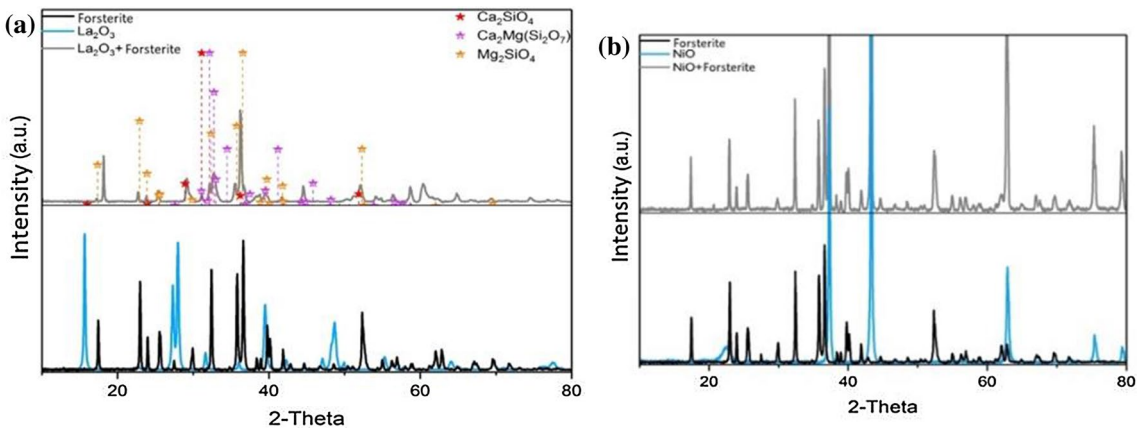


**Figure 8** XRD measurements of oxide mixed pellets for **a** $La_2O_3$ mixed pellets and **b** NiO mixed pellets. The resulting reaction phases are depicted in the figure for intensities greater than 10%.

material are shown in blue and black, respectively. In the upper part of the graph, the oxide mixed pellet of the respective oxide and forsterite sintered at $T = 1300$ °C for 5 h is highlighted in grey. More information can be found in the Supporting Information 4 (Table 4).

Both measurements display that neither $La_2O_3$ nor NiO show any significant reactivity toward forsterite, since in case of $La_2O_3$, the phases formed after heat treatment do not contain La. In case of the elements of the titanium-based perovskites STO, STF25 and CTF, the oxides show a total different reactivity. In case of $Fe_2O_3$, for instance, the EDS mapping of the double-layered pellet displays the formation of two reaction layers after heat treatment. This is comparable to the reaction layers visible for CTF-forsterite and STF25-forsterite, respectively (Fig. 2). In addition, the majority of Zn and Ca is again found within this reaction layer. The reaction layers of the $Fe_2O_3$ double-layered pellet contains Ca, Mg, Zn and Fe and Ca, Zn and Fe, respectively. An analysis of the oxide double-layered pellets leads to the same conclusion as the one from the electrode–forsterite combinations: Zn and Ca are distributed across the whole oxide each time. These findings are supported by Matte et al., describing zinc as the most volatile of the used elements. This results in a distribution of Zn even outside of the forsterite layer. CaO, on the other hand, is known for the formation of mixed oxide phases with $La_2O_3$ at temperatures around 1000 °C, which here, again, explains that Ca appears even outside of the forsterite layer [30]. These results can be confirmed by all the metal oxides investigated within this study. Further XRD measurements, summed up in Table 5, serve to underline the formation of reaction phases for $Fe_2O_3$, SrO and CaO (*cf.* Supplementary 4). The determination of the foreign phases has been determined by comparing with ICSD. With these oxides, the foreign phases that are formed contain Mg and / or Si, thereby underlining the reactivity of Mg and Si from the forsterite support material. Here, again, these findings are in good agreement with the results obtained from EDS electrode–forsterite combinations.

**Table 4** Electrode–forsterite combinations and their formed phases after the standard heat treatment

| Electrode–forsterite | Foreign phases formed | |
|---|---|---|
| L4N3-forsterite | $La_9Mg_{0.5}Si_6O_{26}$ | $La_2NiO_{4.003}$ |
| L3N2-forsterite | $La_9Mg_{0.5}Si_6O_{26}$ | |
| STO-forsterite | | |
| STF25-forsterite | $Sr_2Mg(Si_2O_7)$ | $Fe_2MgO_4$ |
| CTF-forsterite | $CaMgSiO_4$ | $Fe_2MgO_4$ |

The spectra are shown in the supplementary section (cf. Supplementary 3) (the determination of the foreign phases has been determined by comparing with ICSD)

## Electrochemical characterization

### *Electrochemical impedance measurements*

EIS was used to measure the performance of each electrode material in terms of the respective polarization resistance. A well-performing electrode is therefore indicated by low polarization resistance ($R_{pol}$). Within this research, we were looking for an electrode suitable for a low-cost co-firing manufacturing route, which also displays good performance while in contact with forsterite. In this context, two different symmetrical cell setups were used ("pure" and "mixed"), in order to investigate the influence of forsterite in regard with the formation of secondary phases and consequently, the electrochemical performance of the cell. As described above, only $R_{pol}$ is of interest for evaluating the electrode materials and consequently, $R_{ohm}$ was subtracted in the Nyquist plots (Figs. 9 and 10). The "mixed" cell setup represents a kind of worst-case scenario as both materials, the forsterite and the

**Table 5** Listing of the different oxide mixed-pellets and their respective foreign phases formed with forsterite after the standard heat-treatment (the determination of the foreign phases has been determined by comparing with ICSD)

| Mixed-pellets | Foreign phases formed | | |
|---|---|---|---|
| $Fe_2O_3$ | $(Mg_{0.06}Fe_{0.94})$ $Mg_{0.14}(Fe_{0.77}Mg_{1.23})O_4$ | $Mg_{1.83}Fe_{0.17}(SiO_4)$ | $MgSiO_3$ |
| SrO | $Sr_2SiO_4$ | $Sr_3MgSi_2O_8$ | $Sr_3O(SiO_4)$ |
| CaO | $Ca_2SiO_4$ | $Ca_3Mg(SiO_4)_2$ | MgO |
| $La_2O_3$ | $Ca_2SiO_4$ | $Ca_2Mg(Si_2O_7)$ | $Mg_2SiO_4$ |

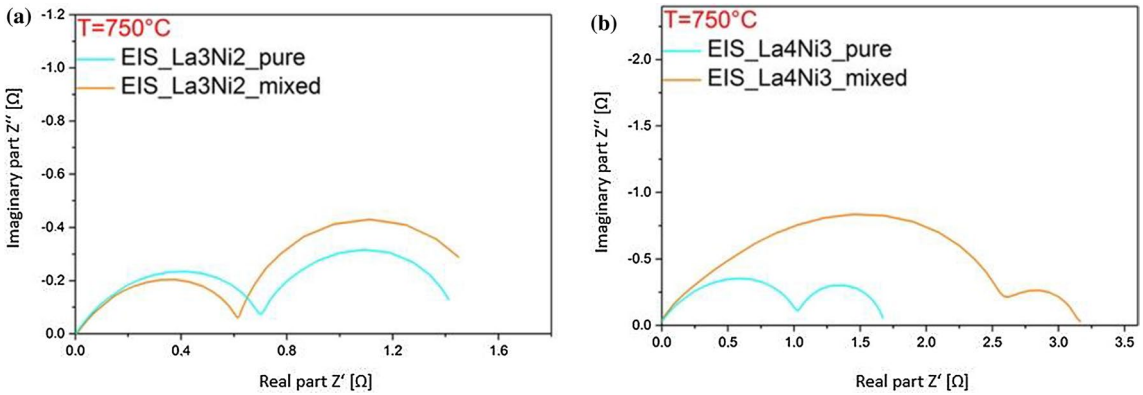


**Figure 9** Nyquist plots of the EIS_electrode_pure (blue) and EIS_electrode_mixed (orange) samples at $T = 750$ °C for the electrodes **a** L4N3 and **b** L3N2. Note the differences in the scaling of the x-axis. The Nyquist plots of the other electrodes are listed in Supplementary 5. ($R_{ohm}$ is subtracted. For interpretation of the references to color in this figure legend, the reader is referred to the Web version of this article).

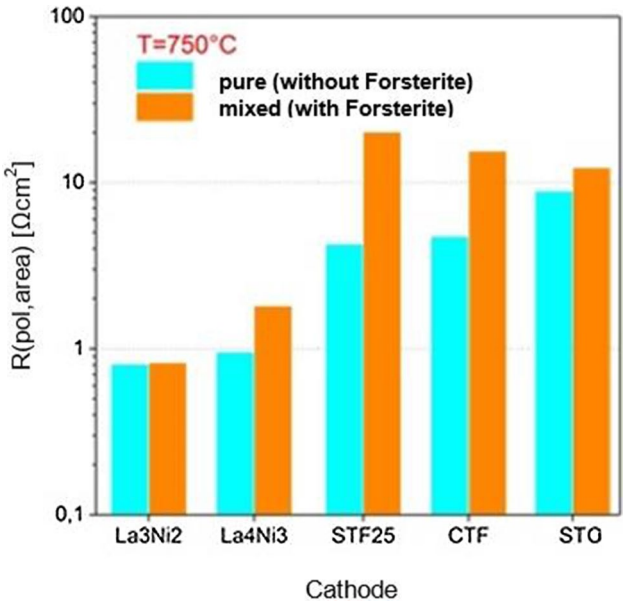


**Figure 10** Bar chart of the $R_{(pol;area)}$ values for the EIS_electrode_pure and EIS_electrode_mixed samples.

respective electrode material, were mixed together to enlarge the available interaction volume between both materials. In a "real" cell architecture only a plane interface between both layers would exist. Figure 10 shows both the Ruddlesden–Popper phase material and the titanium-based perovskite phase materials with the same trend: The samples with a "mixed" CCL display a (slightly) higher $R_{pol}$ value (the $R_{pol}$ is represented by the intercept where the Nyquist plot cuts the $x$-axis). The $R_{pol}$ values can then be related to the active surface area of the sample ($D = 12$ mm; $A = 1.1$ cm$^2$) by applying the following formula: $R_{pol}$ (Ω) * A/2 (cm$^2$) = $R_{pol;area}$ (Ωcm$^2$). These $R_{pol;area}$ values are listed in Fig. 10 for all of the examined electrodes. It should be noted that the "pure" $R_{pol;area}$ values of L4N3 (0.94 Ω cm$^2$) and L3N2 (0.80 Ω cm$^2$) are both better than the best of the previous reported ones from our group (LSF: 0.96 Ω cm$^2$). As a comparison, the best "mixed" $R_{pol;area}$ value is obtained for LSF: 0.25 Ωcm$^2$ (L4N3: 1.79 Ωcm$^2$ and L3N2: 0.81 Ωcm$^2$)[32]. With respect to the interaction tests of the above-mentioned electrodes with forsterite, these results are congruent with the formation of secondary phases, due to contact with forsterite. While air-electrode materials, such as L3N2 or STO, with the formation of either none or only one secondary phase, show only little changes in the measured $R_{pol;area}$ values, this changes completely when more secondary phases are formed; indeed, the value for L4N3 is nearly double.

### *Cross-sectional characterization of the electrodes by SEM*

For a better insight into the huge differences within the measured $R_{pol;area}$ values of the electrode materials, cross sections of each of the electrode samples after EIS measurements were prepared and investigated. Hereby, next to the formation of foreign phases, it is especially the electrode densification, which is of great interest. From Fig. 11 and Table 6, it can be seen that L4N3 (32 vol%) and L3N2 (33 vol%) have a slightly higher porosity and therefore a less density than the titanium-based perovskites, in case of the "pure" samples. However, this changes when

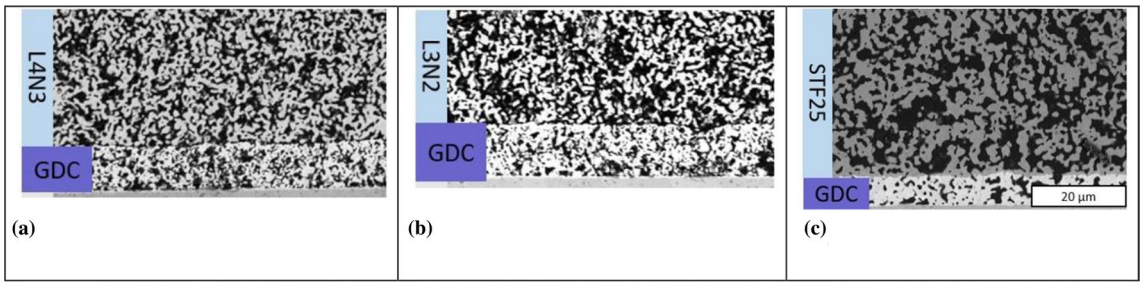


**Figure 11** Cross sections of the EIS samples: 8YSZ (grey), GDC barrier-layer (purple) substrates with different electrode layers (blue): **a** L4N3, **b** L3N2 and **c** STF25. (For interpretation of the references to color in this figure legend, the reader is referred to the Web version of this article).

**Table 6** Porosity values in % of the different electrode materials

| Electrode material | Without forsterite ("pure") Porosity (%) | With forsterite ("mixed") Porosity (%) |
|---|---|---|
| L4N3 | 32 | 28 |
| L3N2 | 33 | 27 |
| STO | 28 | 28 |
| STF25 | 25 | 39 |
| CTF | 23 | 21 |

comparing the "mixed" samples: Here, STF25 is the least dense material (39 vol% porosity). As the particle size of the inks was kept constant (focus on the respective $d_{50}$ values above), this result highlights the difference in the sinterability of the utilized materials. It is known from the literature that the electrocatalytically active surface area has a drastic impact on the $R_{(pol;area)}$ [37]. It should be noted that in none of the here reported electrodes, a post-densification of GDC was observed. This is in good agreement with the results previously reported in our group that mostly Co is responsible for the observable post-densification of GDC [32].

Only in case of STF25, an additional foreign phase was observed containing Sr, Zr and O. We assume that it corresponds to $SrZrO_3$. In the literature, this phase is known to be electrically insulating. It should be noted that the $R_{(pol;area)}$ values correlate with the formation of the secondary phase beneath the GDC layer. It seems that a continuous Sr–Zr–O layer drastically affects the $R_{(pol;area)}$ [32].

## Discussion

A certain reaction has been exhibited in all of the here reported electrode–forsterite combinations. While STF25 (7.0 µm; Sr–Si–Ca–Mg–Zn), CTF (8.1 µm; Si–Ca–Mg–Zn) and the two Ruddlesden–Popper phases (L4N3: 6.2 µm: La–Ni–Zn and L3N2: 4.3 µm: La–Ni–Zn) show formation of a reaction layer, this is not the case for STO. L4N3 and L3N2 show foreign phases with an enrichment of Mg, Ni and Zn. This diffusion of the elements can be explained by different reasons, such as thermal, electrical or chemical potential gradient and is in good agreement with the literature [38, 39]. Furthermore, the elements of the electrode phase and the forsterite material are eager to reach a thermodynamically stable state, in which they are in equilibrium. This can be shown by the diffusion tendency of the elements in TEM lamella point analysis of L3N2 in Fig. 5. Additionally, La from the A-site of the two perovskite materials do not show any tendency to react with forsterite. These results are supported by the individual oxide measurements (*cf.* Figure 7 and Supplementary 3) as well as by the EDS mappings of the double-layered single oxide pellets of $La_2O_3$ with forsterite (*cf.* Table 5 and Supplementary 4). These tests were undertaken to identify elements, which do not react with the support material. The results from these EDS mappings and XRD measurements show the non-reactivity of $La_2O_3$, since no foreign phases nor any reaction layer can be found after heat treatment at T = 1300 °C for 5 h. Moreover, NiO also does not show any reactivity toward forsterite. However, both L4N3 and L3N2, which are only made out of the three elements La, Ni and O, show little reactivity toward forsterite and consequently low tendency of diffusion. While STO also reveals only little

formation of foreign phases, which are actually too few for the detection limit of the XRD measurements, STF25 and CTF show the highest diffusion tendency within this row. This can be explained by the strong reaction tendency of the three elements Sr, Ca and Mg. This is in good agreement with the above mentioned performed EDS mappings of the double-layered single oxide pellets of SrO and CaO as well as the former reported publications by our group [31, 32].

The XRD measurements of the respective electrode materials after synthesis and heat treatment at $T = 1300$ °C show another result. Except STO, all of the here reported electrode materials react with forsterite, indicating that the degradation of the electrode material is not the only reason for the formation of foreign phases and / or reaction layers. It is known in the literature that cation mobility—due to compositional gradients within the examined material—at high temperatures is given as a possible reason for the demixing and decomposition, ultimately resulting in the formation of new phases [40, 41]. In case of STF25, another effect comes into play: Gheitanchi and co-workers investigated the integration of different elements into the forsterite–olivine-structure underlining the reactivity of Sr and forsterite. Excess Sr leads to the formation of $Sr_2MgSi_2O_7$, which was obtained for the electrode–forsterite mixture of STF25. Last but not least, it should be noted that the number of foreign phases is not related to high temperature stability of the respective electrode material [42].

The two "pure" Ruddlesden–Popper material phases L4N3 and L3N2 show the lowest polarization resistance $R_{pol;area}$ (0.94 $\Omega cm^2$ in case of L4N3 and 0.80 $\Omega cm^2$ in case of L3N2) within this row, investigated and reported by our group. However, this changes when the investigated support material forsterite comes into play. In that case, LSF has the lowest $R_{pol;area}$: 0.25 $\Omega cm^2$, compared to 1.79 $\Omega cm^2$ for L4N3 and 0.81 $\Omega cm^2$ for L3N2. The general trend that the polarization resistance increases through addition of forsterite is also confirmed by the results reported here earlier [31, 32].

Due to the strong thermodynamic stability of L4N3 and L3N2, the perovskite structure will not decompose at higher temperature and consequently the catalytic properties keep constant. This can be confirmed by the XRD measurements. Both the polarization resistance of the "pure" and the "mixed" L4N3 and L3N2 shows values around 1 $\Omega cm^2$, which are in the same range as those found in the literature (0.30 $\Omega cm^{-2}$ at 700 °C for L4N3 and L3N2). This slight difference of the polarization resistance can be explained by different synthesis routes or the production route of the cell, which has been reported in the literature before [43]. Another reason might be differences in the sample's porosity. The increased polarization resistance of the "mixed" L4N3, on the other hand, can be explained by the formation of additional L3N2 at higher temperatures, preventing to form a uniform layer of only L4N3.

In case of the five electrode materials here reported, only STF25 shows the formation of a foreign phase: a continuous thin layer of $SrZrO_3$, which is known to be an insulator. Consequently, the polarization resistance doubles when adding forsterite. This can be explained by Szász and co-workers saying that a $SrZrO_3$ layer continuity of > 95% is reported to have a critical impact upon the $R_{pol}$ [44, 45].

## Conclusions

We have investigated five potential air-electrode materials in regard of their reactivity toward the support material forsterite. The forsterite-based solid oxide cell would exhibit co-sinterability and thus low-cost manufacture ability. The materials can be divided into the two groups: Ruddlesden–Popper phases and titanium-based perovskites. The two Ruddlesden–Popper phase materials L3N4 and L3N2 show very good thermodynamic stability and moderate reaction tendency toward forsterite, leading to little foreign phases in either the electrode–forsterite phase or in the electrode phase. In contrast, the three titanium-based perovskites display a different reactivity: While STO is the most stable phase material, the other two perovskites STF25 and CTF show high reactivity toward forsterite, resulting in foreign phases in the two phases, forsterite and electrode, as well as on the interface. These findings were characterized by SEM, XRD, EDS and TEM lamella point analysis. Si, Sr and Zn are mostly responsible for the formation of the reaction layers and the foreign phases. La and Ni, on the other hand, did not show any reactivity toward forsterite after heat treatment of the respective oxide, double-layered and mixed pellets and the perovskite materials containing either La or Ni.

In case of the electrochemical impedance spectroscopy (EIS), once again L4N3 and L3N2 show the best

results in respect to the polarization resistance. However, this situation changes when investigating the interaction of these two materials with forsterite. The titanium-based perovskites STO, STF25 and CTF, on the other hand, show relatively high polarization area resistance, which is in case of STF25 caused by the formation of a continuous thin layer of $SrZrO_3$. Compared to conventional cathode materials, only LSF shows lower polarization resistance, which is especially the case considering the interaction with forsterite [31, 32]. Consequently, the two Ruddlesden–Popper phase materials are of great interest for possible further investigations and possible tests of full solid oxide cells. However, due to the end of the research project, no further material was available.

## Supplementary

The SEM images in the supplementary part show light to heavy washout, as no further corrections could be made by the machine.

## Acknowledgements

The authors like to thank Robert Bosch GmbH for providing the forsterite base materials and the German Federal Ministry for Economic Affairs and Climate Action (BMWK) for funding (contract No. 03ET6101).

## Author Contributions

Most of the experimental design and the measurements for the characterization were done by FG. MJ was responsible for further experimental design, conception and manuscript composition. SZ and YJS were responsible for further carrying out measurements, such as EDS and XRD. OG and NM were also responsible for conception and manuscript composition.

## Funding

Open Access funding enabled and organized by Projekt DEAL.

## Data and code availability

All the experimental data within this article should be available to the readers and can be found in it. No additional information is needed.

## Declarations

**Conflict of interest** There are no conflicts of interest to declare.

**Ethical approval** No human tissue or cells were needed for carrying out the above-described experiments.

**Supplementary Information** The online version contains supplementary material available at https://doi.org/10.1007/s10853-023-08862-0.



## References

[1] Ruddlesden SN, Popper P (1958) The compound $Sr_3Ti_2O_7$ and its structure. Acta Crystallogr 11:54–55

[2] Ruddlesden SN, Popper P (1957) New compounds of the $K_2NiF_4$ type. Acta Crystallogr 10:538–539

[3] Yatoo MA, Skinner SJ (2022) Ruddlesden–Popper phase materials for solid oxide fuel cell cathodes: a short review. Mater Today Proc 56:3747–3754

[4] Birol T, Benedek NA, Fennie CJ (2011) Interface control of emergent ferroic order in Ruddlesden–Popper $Sr_{\{n+1\}}Ti_{\{n\}}O_{\{3n+1\}}$. Phys Rev Lett 107:257602–257606

[5] Oh YS, Luo X, Huang FT, Wang Y, Cheong SW (2015) Experimental demonstration of hybrid improper ferroelectricity and the presence of abundant charged walls in (Ca, $Sr_)3T_i2_O7$ crystals. Nat Mater 14:407–413

[6] Dwivedi A, Cormack AN (1991) Crystal chemistry of Ruddlesden–Popper type structures in high $T_c$ ceramic superconductors. Bull Mater Sci 14:575–584

[7] Woolley RJ, Skinner SJ (2014) Functionally graded composite $La_2NiO_{4+\delta}$ and $La_4Ni_3O_{10-\delta}$ solid oxide fuel cell cathodes. Solid State Ion 255:1–5

[8] Battle PD, Blundell SJ, Green MA, Hayes W, Honold M, Klehe AK, Laskey NS, Millburn JE, Murphy L, Rosseinsky MJ, Samarin NA, Singleton J, Sluchanko NE, Sullivan SP, Vente JF (1996) Colossal magnetoresistance in $Sr_2NdMn_2O_7$; $MnO_6$ (x=0.0, 0.1). J Phys Condens Matter 8:L427–L434

[9] Nirala G, Yadav D, Upadhyay S (2020) Ruddlesden–Popper phase $A_2BO_4$ oxides: recent studies on structure, electrical, dielectric, and optical properties. J Adv Ceram 9:129–148

[10] Choi S, Yoo S, Shin J-Y, Kim G (2011) High performance SOFC cathode prepared by infiltration of $La_{n+1}Ni_nO_{3n+1}$ ($n$ = 1, 2, and 3) in porous YSZ. J Electrochem Soc 158:B995–B999

[11] Amow G, Davidson IJ, Skinner SJ (2006) A comparative study of the Ruddlesden–Popper series, $La_{n+1}Ni_nO_{3n+1}$ ($n$ = 1, 2 and 3), for solid-oxide fuel-cell cathode applications. Solid State Ion 177:1205–1210

[12] Takahashi S, Nishimoto S, Matsuda M, Miyake M (2010) Electrode properties of the Ruddlesden–Popper series, $La_{n+1}Ni_nO_{3n+1}$ ($n$=1, 2, and 3), as intermediate-temperature solid oxide fuel cells. J Am Ceram Soc 93:2329–2333

[13] Burriel M, Garcia MG, Rossell M, Figueras A, Van Tendeloo G, Santiso J (2007) Enhanced high-temperature electronic transport properties in nanostructured epitaxial thin films of the $La_{n+1}Ni_nO_{3n+1}$ Ruddlesden−Popper series ($n$ = 1, 2, 3, ∞). J Chem Mater 19:4056–4062

[14] Skinner SJ, Kilner JA (2000) Oxygen Diffusion and Surface Exchange in $La_{2-x}Sr_xNiO_{4+\delta}$. Solid State Ion 135:709–712

[15] Wan J, Goodenough JB, Zhu JH (2007) $Nd_{2-x}LaxNiO_{4+\delta}$, a mixed ionic/electronic conductor with interstitial oxygen, as a cathode material. Solid State Ion 178:281–286

[16] Kharton VV, Figueiredo FM, Navarro L, Naumovich EN, Kovalevsky AV, Yaremchenko AA, Viskup AP, Carneiro A, Marques FMB, Frade JR (2001) Ceria-based materials for solid oxide fuel cells. J Mater Sci 36:1105–1117. https://doi.org/10.1023/A:1004817506146

[17] Kilner JA, Shaw CKM (2002) Mass transport in $La_2Ni_{1-x}Co_xO_{4+\delta}$ Oxides with the $K_2NiF_4$ Structure. Solid State Ion 154:523–527

[18] Boehm E, Bassat JM, Steil MC, Dordor P, Mauvy F, Grenier JC (2003) Oxygen transport properties of $La_2Ni_{1-x}Cu_xO_{4+\delta}$ mixed conducting oxides. Solid State Sci 5:973–981

[19] Aguadero A, Alonso JA, Escudero MJ, Daza L (2008) Evaluation of the $La_2Ni_{1-x}CuxO_{4+\delta}$ system as SOFC cathode material with 8YSZ and LSGM as electrolytes. Solid State Ion 179:393–400

[20] Lou Z, Peng J, Dai N, Qiao J, Yan Y, Wang Z, Wang J, Sun K (2012) High performance $La_3Ni_2O_7$ cathode prepared by a facile sol-gel method for intermediate temperature solid oxide fuel cells. Electrochem Commun 22:97–100

[21] Amow G, Skinner SJ (2006) Recent developments in Ruddlesden–Popper nickelate systems for solid oxide fuel cell cathodes. J Solid State Electrochem 10:538–546

[22] Tsipis EV, Patrakeev MV, Waerenborgh JC, Pivak YV, Markov AA, Gaczynski P, Naumovich EN, Kharton VV (2007) Oxygen non-stoichiometry of $Ln_4Ni_{2.7}Fe_{0.3}O_{10-\delta}$ ($Ln$=La, Pr). J Solid State Chem 180:1902–1910

[23] Brett DJL, Atkinson A, Brandon NP, Skinner SJ (2008) Intermediate temperature solid oxidefuelcells. Chem Soc Rev 37:1568–1578

[24] Menzler NH, Tietz F, Uhlenbruck S, Buchkremer HP, Stöver D (2010) Materials and manufacturing technologies for solid oxide fuel cells. J Mater Sci 45:3109–3135. https://doi.org/10.1007/s10853-010-4279-9

[25] Menzler NH, Schafbauer W, Han F, Buchler O, Mucke R, Buchkremer HP, Stöver D (2010) Development of high power density solid oxide fuel cells (SOFCs) for long-term operation. In: Nie JF, Morton A (eds) PRICM 7, 1–3, pp 2875–2878

[26] Roehrens D, Packbier U, Fang Q, Blum L, Sebold D, Bram M, Menzler N (2016) Operation of thin-film electrolyte metal-supported solid oxide fuel cells in lightweight and stationary stacks. Mater Microstruct Aspects Mater 9:762–768

[27] Brandon NP, Corcoran D, Cummins D, Duckett A, El-Khoury K, Haigh D, Leah R, Lewis G, Maynard N, McColm T, Trezona R, Selcuk A, Schmidt M (2013) Development of metal supported solid oxide fuel cells for operation at 500–600 °C. J Mater Eng Perform 22:2900–2903

[28] Brandner M, Bram M, Froitzheim J, Buchkremer HP, Stöver D (2008) Electrically conductive diffusion barrier layers for metal-supported SOFC. Solid State Ionics 179:1501–1504

[29] Quadakkers WJ, Piron-Abellan J, Shemet V, Singheiser L (2003) Metallic interconnectors for solid oxide fuel cells—a review. Mater High Temp 20:115–127

[30] Matte E, Holzlechner G, Epple L, Stolten D, Lupetin P (2019) Impact of silicate substrate and cosintering on cathode performance in an inert substrate-supported solid oxide fuel cell. J Power Sources 413:334–343

[31] Grimm F, Menzler NH, Guillon O (2020) Selection of cathode materials for forsterite supported solid oxide fuel cells—part i: materials interactions. J Power Sources 451:227607–227617

[32] Grimm F, Neubert K, Karl J, Menzler NH, Guillon O (2020) Selection of cathode materials for forsterite-supported solid oxide fuel cells—part II: electro-catalytic activity. J Power Sources 451:227811–227821

[33] Huízar-Félix AM, Hernández T, de la Parra S, Ibarra J, Kharisov B (2012) Sol-gel based pechini method synthesis and characterization of $Sm_{1-x}CaxFeO_3$ Perovskite 0.1 ≤ x ≤ 0.5. Powder Technol 229:290–293

[34] Danks AE, Hall SR, Schnepp Z (2016) The evolution of 'sol–gel' chemistry as a technique for materials synthesis. Mater Horiz 3:91–112

[35] Schulze-Küppers F, Donkelaar SFP, Baumann S, Prigorodov P, Sohn YJ, Bouwmeester HJM, Meulenberg WA, Guillon O (2015) Structural and functional properties of $SrTi_{1-x}Fe_xO_{3-\delta}$ (0≤x≤1) for the use as oxygen transport membrane. Sep Pur Technol 147:414–421

[36] Liu P, Han N, Wang W, Ran R, Zhou W, Shao Z (2021) High-quality Ruddlesden–Popper Perovskite film formation for high-performance Perovskite. Solar Cells Adv Mater 33:2002582–2002622

[37] Dang D, Li X, Lai SY, Gerdes K, Liu M (2014) Enhancing SOFC cathode performance by surface modification through infiltration. Energy Environ Sci 7:552–575

[38] van Doorn RHE, Bouwmeester HJM, Burggraaf AJ (1998) Kinetic decomposition of $La_{0.3}Sr_{0.7}CoO_{3-\delta}$ perovskite membranes during oxygen permeation. Solid State Ion 111:263–272

[39] Lein HL, Wiik K, Grande T (2006) Kinetic demixing and decomposition of oxygen permeable membranes. Solid State Ion 177:1587–1590

[40] Wærnhus I, Sakai N, Yokokawa H, Grande T, Einarsrud M-A, Wiik K (2004) Mass transport in $La_{1-x}Sr_xFeO_3$($x$=0 and 0.1) measured by SIMS. Solid State Ion 175:69–71

[41] Wang B, Zydorczak B, Wu Z-T, Li K (2009) Stabilities of $La_{0.6}Sr_{0.4}Co_{0.2}Fe_{0.8}O_{3-\delta}$ oxygen separation membranes—effects of kinetic demixing/decomposition and impurity segregation. J Membr Sci 344:101–106

[42] Gheitanchi R, Kharaziha M, Emadi R (2017) Sr-doped forsterite nanopowder: synthesis and biological properties. Ceram Int 43:12018–12025

[43] Guo Y-Q, Yin Y-M, Tong Z, Yin J-W, Xiong M-W, Ma., Z.-F. (2011) Impact of synthesis technique on the structure and electrochemical characteristics of $Pr_{0.6}Sr_{0.4}Co_{0.2}Fe_{0.8}O_{3-\delta}$ (PSCF) cathode material. Solid State Ion 193:18–22

[44] Wilde V, Stormer H, Szasz J, Wankmüller F, Ivers-Tiffee E, Gerthsen D (2018) $Gd_{0.2}Ce_{0.8}O_2$ diffusion barrier layer between $(La_{0.58}Sr_{0.4})(Co_{0.2}Fe_{0.8})O_{3-\delta}$ cathode and $Y_{0.16}Zr_{0.84}O_2$ electrolyte for solid oxide fuel cells: effect of barrier layer sintering temperature on microstructure. ACS Appl Energy Mater 1:6790–6800

[45] Szasz J, Wankmüller F, Wilde V, Störmer H, Gerthsen D, Menzler NH, Ivers-Tiffee E (2018) Nature and functionality of $La_{0.58}Sr_{0.4}Co_{0.2}Fe_{0.8}O_{3-\delta}/Gd_{0.2}Ce_{0.8}O_{2-\delta}/Y_{0.16}Zr_{0.84}O_{2-\delta}$ interfaces in SOFCs. J Electrochem Soc 165:F898–F906